HAL
open science

The 2003 December 26 Bam earthquake (Iran), Mw 6.6, aftershock sequence.

M. Tatar, Denis Hatzfeld, A. Moradi, Anne Paul

To cite this version:

M. Tatar, Denis Hatzfeld, A. Moradi, Anne Paul. The 2003 December 26 Bam earthquake (Iran), Mw 6.6, aftershock sequence.. Geophysical Journal International, 2005, 163 (1), pp.90-105. 10.1111/j.1365-246X.2005.02639.x . hal-00110027

HAL Id: hal-00110027

https://hal.science/hal-00110027

Submitted on 19 Feb 2021

HAL is a multi-disciplinary open access archive for the deposit and dissemination of scientific research documents, whether they are published or not. The documents may come from teaching and research institutions in France or abroad, or from public or private research centers.

L'archive ouverte pluridisciplinaire **HAL**, est destinée au dépôt et à la diffusion de documents scientifiques de niveau recherche, publiés ou non, émanant des établissements d'enseignement et de recherche français ou étrangers, des laboratoires publics ou privés.

Geophys. J. Int. (2005) **163,** 90–105 doi: 10.1111/j.1365-246X.2005.02639.x

The 2003 December 26 Bam earthquake (Iran), *Mw* 6.6, aftershock sequence

M. Tatar,[1] D. Hatzfeld,[2] A. S. Moradi[1] and A. Paul[2]

[1] *International Institute of Earthquake Engineering and Seismology, Tehran, Iran*
[2] *Laboratoire de Géophysique Interne et Tectonophysique, Grenoble, France. E-mail: denis.hatzfeld@ujf-grenoble.fr*

Accepted 2005 March 10. Received 2005 March 8; in original form 2004 November 19

SUMMARY

From 2003 December 29 to 2004 January 30, a dense seismological network of 23 stations was installed in the epicentral area of the 2003 December 26 Bam earthquake to study the aftershock seismicity. We select the 331 earthquakes recorded at a minimum of 10 stations, with rms less than 0.1 s and uncertainties less than 1 km, to infer the precise geometry of the seismicity in the fault region. We also process the data with the Double Difference technique to confirm the results. The aftershock cluster is 25 km long, trends north–south, and is located 5 km west of the Bam-Baravat escarpment, exactly beneath the observed surface breaks. At depth, aftershocks are concentrated between 6 and 20 km, beneath the upper layer of relatively low velocity that experienced the maximum slip, and they dip slightly westward. The southernmost part of the aftershock cluster is narrow and defines the rupture zone that is likely the Bam-Baravat fault at depth. However, it is unlikely that it is connected at surface to the Bam-Baravat escarpment but more likely to the co-seismic ruptures south of Bam. On the contrary, the distribution of the northernmost aftershocks spread into a more complex pattern, which is consistent with a northward propagation of the rupture along the fault plane. The focal mechanisms are consistent with right-lateral strike-slip faulting on N–S trending faults, parallel to the Bam-Baravat escarpment.

Key words: aftershocks, Bam earthquake.

GJI Seismology

Downloaded from https://academic.oup.com/gji/article/163/1/90/739453 by guest on 19 February 2021

INTRODUCTION

The Bam earthquake of 2003 December 26, occurred near the southern termination of the N–S trending Nayband and Gowk fault system (Fig. 1) which is located on the west side of the Lut block and accommodates part of the 2.5 cm yr^{-1} northward motion of Arabia relative to Eurasia (Berberian *et al.* 1984; Jackson & McKenzie 1984; Walker & Jackson 2002; Vernant *et al.* 2004). However, the historical (Ambraseys & Melville 1982; Berberian & Yeats 1999) and instrumental (Engdahl *et al.* 1998) seismic activity associated with the Bam-Baravat escarpment itself is rather low and most earthquakes are related to the Nayband, Gowk and Shahdad faults located north of Bam or to the Jiroft fault located in the south. The strongest historical events were the 1864 Khorjand earthquake with an estimated intensity of VIII, the 1854 Chatrood event with a magnitude of $Ms \sim 6$ and the 1897 Kerman-Chatrood earthquake with $Ms \sim 5.5$. The largest instrumental earthquakes are the 1981 June 11 Golbaf earthquake ($Mw = 6.6$), the 1981 July 28 Sirch earthquake ($Mw = 7.1$) and the 1998 March 14 Fandoqa earthquake of magnitude $Mw = 6.6$ (Berberian *et al.* 1984, 2001), all related to the Gowk fault.

The Bam-Baravat escarpment, located east of the city of Bam, is made of three major segments, probably active during the Pleistocene time, trending approximately N–S and ranging from 10- to 30 km long (Berberian 1976; Hessami *et al.* 2004). These different faults, located on the edges of topographic hills, displaced right-laterally geomorphological features. The plain located south and west of Bam is free of any geomorphological signature.

After the December 26 earthquake, no significant surface ruptures were mapped on the Bam-Baravat escarpment fault itself. Only small cracks, in an en-échelon system, were visible along a 5-km-long segment located west of the escarpment, in a region of flat topography (Talebian *et al.* 2004; Hessami *et al.* 2004; Fielding *et al.* 2005). Whether the earthquake was located on a blind fault located to the west (Fielding *et al.* 2005; Talebian *et al.* 2004; Funning *et al.* 2005) or on the Bam-Baravat escarpment itself (Hessami *et al.* 2004; Fu *et al.* 2004) is debated. Teleseismic relocations (hereafter called EHB relocation) of the mainshock and the largest aftershocks epicentres using the Engdahl–Hilst–Buland method (Engdahl *et al.* 1998) were located approximately 15 km southwest of the Bam-Baravat escarpment (Engdahl, personal communication). The CMT solution of the mainshock provided by Harvard was consistent with a pure dextral strike-slip motion on a N–S trending fault.

Initial body-wave modelling of the main shock suggests that the first shock ($Mw \sim 6.5$), whose mechanism is dextral strike-slip, was followed about 9 s later by a second shock ($Mw \sim 5.8$), with a reverse faulting mechanism, located further south (Talebian *et al.* 2004). This complex rupture involving two shocks

 © 2005 RAS

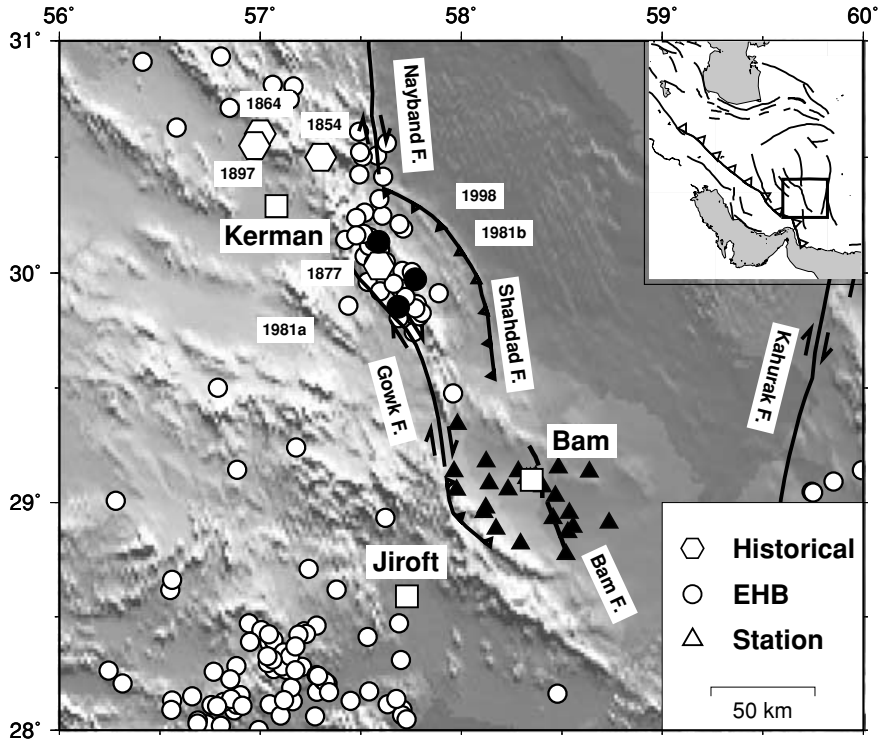

Figure 1. Tectonic map of the Bam area after Walker & Jackson (2002). Historical seismicity is marked as hexagons (Ambraseys & Melville 1982; Berberian & Yeats 1999) and instrumental seismicity as circles (Engdahl *et al.* 1998). The largest instrumental events are plotted as black circles. Stations of the temporary seismological network are shown as black triangles.

with different mechanisms is also consistent with InSAR observations (Talebian *et al.* 2004; Funning *et al.* 2005), which suggest that the second event was located on the Bam-Baravat escarpment itself.

In summary, the precise location of the very destructive Bam earthquake is uncertain by up to 10 km using only teleseismic data and methods. The relationship between the rupture and the Bam-Baravat escarpment and the observed surface breaks is unclear and the rupture history suggests a complex mechanism.

DATA

In order to study the aftershocks of the Bam earthquake, a network of 23 portable three-component stations was deployed around the epicentral area of the main shock starting on 2003 December 28, 3 days after the main shock, for about 1 month (Tatar *et al.* 2004). Because of logistical problems, the network was completed only after January 2 and 3 additional stations were installed in the city of Bam only on January 14.

The 23-station temporary seismological network consisted of 12 CMG-6TD seismometers connected to CMG-DM24 Guralp recorders, and 11 CMG-40T seismometers, connected to MiniTitan recorders. All stations were recording in continuous mode. The CMG-6TD were sampled at 100 Hz, whereas the CMG-40T were sampled at 62.5 Hz. At all stations, the time was calibrated every hour with a GPS receiver. In this paper, we examine the aftershock seismicity between December 31 and January 27. All readings were processed with the Pickev picking software (http://sismalp.obs.ujf-grenoble.fr/ftp-sismalp/msdos/) on the three-component seismograms. We estimate the picking accuracy to be better than 0.05 s in all readings.

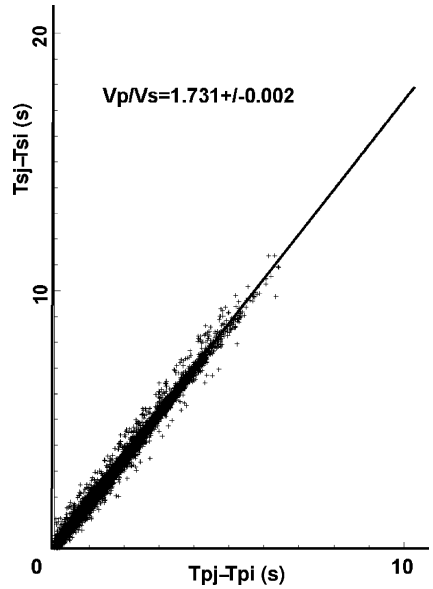

Figure 2. Vp/Vs ratio computed from 9300 arrival times.

We first locate all events in a standard half space model with $Vp = 6.0\ \mathrm{km\,s^{-1}}$ with Hypo71 (Lee & Lahr 1972). Among the 544 events that were recorded during that period of time with uncertainties less than 2 km, we select a subset of 331 events recorded by a minimum of 10 stations, including at least 5 *S* arrival times, with an azimuthal gap less than 180° and a rms value less than 0.1 s and uncertainties both in epicentral (erh) and depth (erz) less than 2 km. This selected set

Downloaded from https://academic.oup.com/gji/article/163/1/90/739453 by guest on 19 February 2021

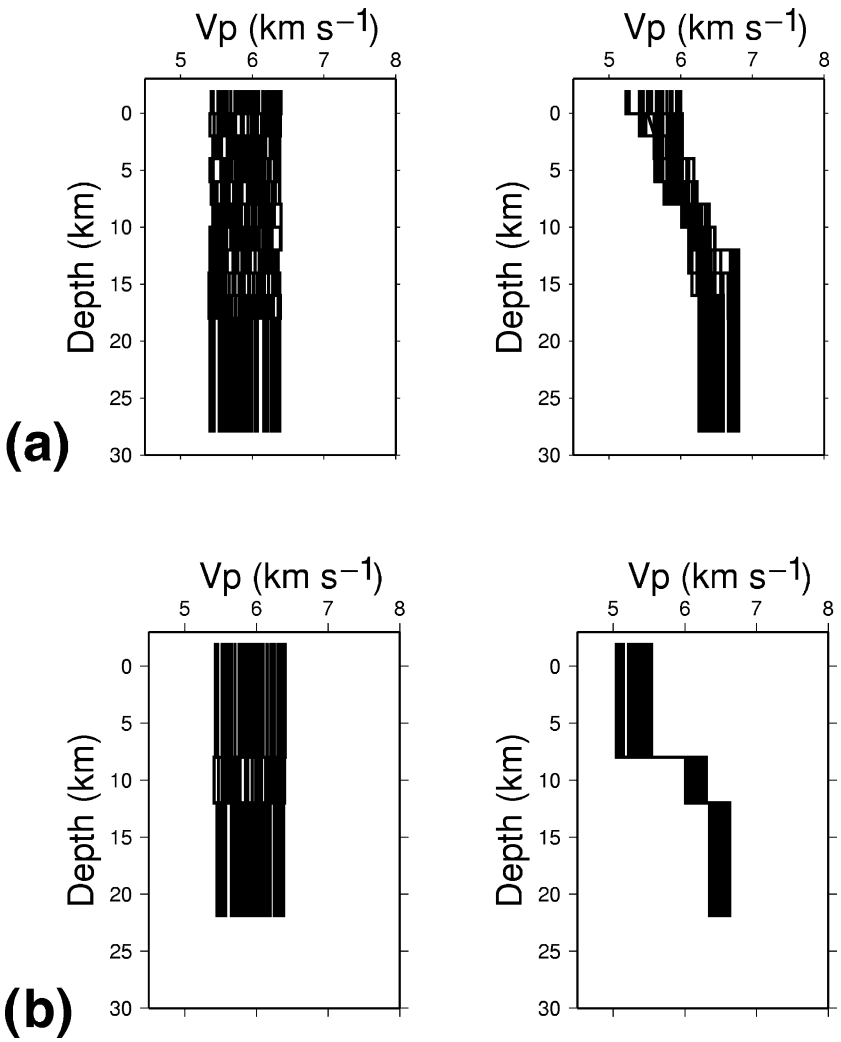

Figure 3. Velocity structure obtained for the shallow crust by 1-D inversion of traveltimes (Kissling 1988) of the 232 selected aftershocks recorded by a minimum of 10 seismological stations. We use 50 randomly distributed starting models (left) that converge to the models plotted in the right hand side. (a) Model with 10 layers, 2 km thick. (b) Simplified three-layer starting model.

of data is used to conduct several tests and compute the appropriate velocity structure.

First, averaging Tsj–Tsi versus Tpj–Tpi for all events and all stations, we compute a mean Vp/Vs ratio of 1.731+/−0.002 with a total of 9300 arrival times (Fig. 2).

Secondly, because we have no detailed information on the velocity structure in the Bam area, we search for an appropriate velocity structure. We invert the arrival times of the selected set of events for a 1-D velocity structure using the program VELEST (Kissling 1988). Because the resulting structure is strongly dependent on the starting velocity model, we explore 50 initial models randomly distributed (with differences as large as 0.5 km s^{-1} in each layer) around our starting model. We keep only the resulting models for which the 1-D inversion converges correctly (e.g. the rms decreases significantly to values less than 0.06 s). We start with a first starting velocity structure composed of a stack of layers 2 km thick, of uniform velocity 5.9 km s^{-1}. This multilayered model allows to locate the largest velocity discontinuities but we do use it to find the final velocity model because the number of unknowns are too large. The result of these inversions (Fig. 3a) suggests that no more than three-layers are required in the starting model (Table 1). The three-layer model is then randomly perturbated, to obtain a set of initial models for the inversions. We compute the final velocity model averaging the results of all inversions that converge (Fig. 3b, Table 1). We also check, with the selected set of data, that the corresponding rms value reduces from 0.11 s for the starting homogeneous model, to 0.08 s for the final three-layer model. The shallowest 8-km-thick layer with velocity 5.4 km s^{-1} is slow but has been evidenced in most of our surveys in Iran. It might represent the correction due to the shallow sedimentary layer. Anyway, it is the minimum misfit model that explains our arrival times.

Table 1. Velocity structure, result of the inversion 1-D.

Top of the layer (km)	*P* velocity (km s^{-1})
0	5.30 ± 0.16
8	6.17 ± 0.10
12	6.49 ± 0.08

Lower hemisphere fault plane solutions of single events are determined from a minimum of 12 first-motion polarities (Table 2 and Appendix). Because of the large amount of data following these criteria (206) we used the FPFIT and FPPLOT softwares (Reasen-

Downloaded from https://academic.oup.com/gji/article/163/1/90/739453 by guest on 19 February 2021

Table 2. Parameters for the focal mechanisms.

Nb	Date	Time	Lat	Lon	Depth	Az1	Pl1	de1	Az2	Pl2	de2	Azp	dep	Azt	det	Q
46	311203	14:57	29.073	58.355	15.12	235	85	10	144.1	80.0	175	9.2	3.6	99.9	10.8	B
47	311203	15:43	29.068	58.356	14.06	−20	80	−160	246.4	70.3	−11	204.6	21.1	112.0	6.6	B
49	311203	21:16	29.090	58.363	15.55	−20	75	−150	241.5	61.1	−17	204.0	31.6	108.3	9.1	B
53	10104	04:05	29.107	58.317	16.93	165	80	−180	75.	90.0	−10	29.6	7.1	120.4	7.1	B
54	10104	08:57	29.070	58.366	14.60	−15	85	−160	253.2	70.1	−5	210.8	17.5	117.5	10.2	A
56	10104	10:06	29.092	58.364	16.39	−15	75	−150	246.5	61.1	−17	209.0	31.6	113.3	9.1	B
57	10104	10:08	29.025	58.367	13.78	−5	45	60	214.2	52.2	117	285.7	3.8	185.7	68.9	B
58	10104	10:23	28.992	58.371	9.85	155	45	120	−64.2	52.2	63	44.3	3.8	144.3	68.9	B
59	10104	10:44	29.034	58.364	12.26	95	80	0	5.	90.0	170	50.4	7.1	319.6	7.1	A
60	10104	10:55	29.027	58.362	17.96	245	85	20	153.2	70.1	175	17.5	10.2	110.8	17.5	A
61	10104	11:48	29.085	58.365	10.17	140	80	−20	233.6	70.3	−169	95.4	21.1	188.0	6.6	B
62	10104	13:43	29.042	58.366	13.16	185	85	−170	94.1	80.0	−5	49.9	10.8	319.2	3.6	A
63	10104	14:02	29.051	58.397	12.48	165	55	110	−47.4	39.7	64	240.9	8.0	125.7	71.8	A
64	10104	16:09	29.070	58.339	16.55	240	60	−30	−13.9	64.3	−146	204.6	41.3	112.2	2.7	B
65	10104	16:52	29.055	58.374	15.66	−10	80	−160	256.4	70.3	−11	214.6	21.1	122.0	6.6	A
67	10104	17:34	29.018	58.344	16.77	240	85	20	148.2	70.1	175	12.5	10.2	105.8	17.5	A
68	10104	17:46	29.087	58.359	12.10	20	45	−50	150.1	57.2	−123	5.6	62.0	262.8	6.7	A
70	10104	17:55	29.102	58.365	9.66	80	60	160	180.3	72.8	32	307.8	8.3	43.5	34.2	B
71	10104	19:42	29.152	58.458	13.78	130	25	−90	−50.0	65.0	−90	220.0	70.0	40.0	20.0	C
73	10104	22:25	29.053	58.361	12.95	135	85	−170	44.1	80.0	−5	359.9	10.8	269.2	3.6	A
75	20104	00:35	29.007	58.368	13.81	130	55	90	−50.	35.0	90	220.0	10.0	40.0	80.0	A
76	20104	01:13	29.070	58.367	11.07	120	60	100	−79.4	31.5	73	202.7	14.5	54.9	73.1	A
78	20104	03:21	29.096	58.358	14.06	65	75	−20	160.4	70.7	−164	22.0	24.7	113.3	2.9	A
79	20104	03:22	29.109	58.357	13.52	260	75	−10	−7.4	80.3	−165	216.9	17.5	125.7	3.7	B
80	20104	04:24	29.032	58.365	11.85	90	80	0	0.	90.0	170	45.4	7.1	314.6	7.1	B
83	20104	05:15	29.010	58.394	10.10	35	90	0	−55.	90.0	180	350.0	.7	260.0	.7	B
84	20104	06:10	29.088	58.361	13.49	−10	70	−140	244.	52.8	−25	213.2	42.0	113.5	10.7	B
86	20104	09:48	29.083	58.382	14.76	165	55	100	−32.1	36.2	76	247.8	9.5	109.3	77.4	B
87	20104	10:00	29.115	58.349	10.12	215	70	−30	−43.8	62.0	−157	173.4	35.1	267.1	5.2	B
88	20104	10:01	29.128	58.331	14.69	55	60	30	−51.1	64.3	146	210.6	12.8	85.8	68.3	B
89	20104	10:20	29.026	58.360	17.15	−10	90	−170	260.	80.0	0	215.0	.7	305.0	.7	A
91	20104	10:34	29.023	58.359	14.26	85	80	0	−5.	90.0	170	40.4	7.1	309.6	7.1	A
93	20104	11:44	29.044	58.364	12.26	85	85	0	−5.	90.0	175	40.1	3.5	309.9	3.5	A
94	20104	12:28	29.087	58.349	15.58	160	50	−140	41.7	60.5	−48	4.7	53.4	103.0	6.1	B
97	20104	15:42	29.143	58.317	14.48	−65	85	−90	115.0	5.0	−90	205.0	50.0	25.0	40.0	C
100	20104	17:55	29.100	58.354	11.64	140	85	150	232.9	60.1	6	190.3	17.0	92.2	24.6	A
101	20104	18:21	29.047	58.368	15.44	240	80	10	148.2	80.2	170	14.1	.1	104.1	14.3	A
103	20104	20:11	29.075	58.357	10.82	40	85	0	−50.	90.0	175	355.1	3.5	264.9	3.5	A
105	20104	20:38	29.035	58.363	12.51	90	80	0	0.	90.0	170	45.4	7.1	314.6	7.1	B
106	20104	20:42	29.054	58.371	14.65	85	85	0	−5.0	89.0	175	40.1	3.5	309.9	3.5	B
108	20104	22:41	29.045	58.384	13.04	65	65	40	−44.5	54.4	149	188.1	6.5	284.6	45.3	A
109	20104	22:52	29.139	58.362	10.09	125	50	120	263.1	48.4	59	194.3	.8	102.3	67.5	B
111	30104	00:39	29.064	58.365	11.98	115	65	80	−42.4	26.8	110	212.5	19.4	5.5	68.4	B
113	30104	01:33	29.058	58.365	15.00	−20	80	−170	248.2	80.2	−10	204.1	14.3	114.1	.1	B
116	30104	01:57	29.044	58.387	13.07	95	50	80	−69.7	41.0	102	192.1	4.5	312.5	81.1	A
117	30104	02:21	29.040	58.368	14.75	0	85	170	90.9	80.0	5	45.8	3.6	315.1	10.8	B
119	30104	02:48	29.090	58.346	15.87	120	65	90	−60.	25.0	90	210.0	20.0	30.0	70.0	B
124	30104	03:25	29.069	58.367	11.35	55	50	−120	−83.1	48.4	−59	257.7	67.5	165.7	.8	B
125	30104	03:27	29.056	58.362	11.42	10	70	−170	−83.5	80.6	−20	231.8	21.0	324.6	7.2	A
129	30104	04:17	29.018	58.399	11.72	135	85	−180	45.	90.0	−5	359.9	3.5	90.1	3.5	A
132	30104	05:21	29.010	58.361	13.03	90	80	0	0.	90.0	170	45.4	7.1	314.6	7.1	B
136	30104	06:34	29.086	58.350	15.37	145	70	−170	51.5	80.6	−20	6.8	21.0	99.6	7.2	A
138	30104	08:02	29.100	58.410	16.13	5	75	−160	269.6	70.7	−16	228.0	24.7	136.7	2.9	A
143	30104	11:52	29.040	58.358	12.76	75	80	20	−18.6	70.3	169	207.0	6.6	299.6	21.1	A
146	30104	14:40	29.062	58.272	17.28	165	60	170	260.	81.4	30	29.0	14.4	126.6	27.3	A
148	30104	15:28	29.042	58.352	13.87	−65	80	20	201.4	70.3	169	67.0	6.6	159.6	21.1	A
150	30104	18:17	29.018	58.354	17.49	145	60	160	245.3	72.8	32	12.8	8.3	108.5	34.2	A
153	30104	18:37	29.070	58.356	14.81	120	55	90	−60.	35.0	90	220.0	.7	310.0	.7	A
154	30104	18:54	29.108	58.347	10.74	35	90	−20	125.	70.0	−180	350.0	.7	260.0	.7	B
155	30104	19:50	29.117	58.352	14.10	−30	85	−140	235.8	50.2	−7	200.9	31.0	96.0	23.1	A
156	30104	20:21	29.087	58.353	13.30	105	70	180	195.	90.0	20	328.2	14.0	61.8	14.0	B
157	30104	21:02	29.078	58.353	11.09	−5	80	−160	261.4	70.3	−11	219.6	21.1	127.0	6.6	A
158	30104	21:28	29.080	58.384	13.58	−5	50	−170	258.5	82.4	−40	208.6	33.3	313.3	21.1	A
159	30104	21:47	29.010	58.370	11.38	235	70	−30	−23.8	62.0	−157	193.4	35.1	287.1	5.2	A
161	30104	22:28	29.077	58.347	15.12	230	65	−20	−31.3	71.9	−154	191.0	31.1	98.2	4.6	A

Downloaded from https://academic.oup.com/gji/article/163/1/90/739453 by guest on 19 February 2021

Table 2. (*Continued.*)

Nb	Date	Time	Lat	Lon	Depth	Az1	Pl1	de1	Az2	Pl2	de2	Azp	dep	Azt	det	Q
164	30104	23:39	29.008	58.366	11.54	50	65	−130	−66.7	46.0	−36	272.2	52.1	167.6	11.1	A
170	40104	07:53	29.034	58.366	13.42	10	55	−80	172.9	36.2	−104	5.4	7.2	98.2	21.0	A
172	40104	09:43	29.011	58.358	11.91	−20	85	−160	248.2	70.1	−5	205.8	17.5	112.5	10.2	A
173	40104	10:57	29.008	58.392	9.75	50	80	−20	143.6	70.3	−169	5.4	21.1	98.0	6.6	B
174	40104	12:31	29.007	58.392	9.62	35	90	0	−55.	90.0	180	350.0	.7	260.0	.7	B
176	40104	14:14	29.042	58.362	7.27	85	75	0	−5.	90.0	165	41.0	10.5	309.0	10.5	B
178	40104	15:08	29.003	58.363	10.96	20	70	−160	−77.1	71.3	−21	241.2	28.0	331.6	.8	A
179	40104	15:11	29.112	58.335	13.32	55	55	−40	170.7	58.2	−138	24.5	51.1	292.2	1.9	A
181	40104	15:39	29.078	58.381	13.48	70	45	−50	200.1	57.2	−123	55.6	62.0	312.8	6.7	B
182	40104	16:31	29.128	58.342	7.42	10	80	−170	−81.8	80.2	−10	234.1	14.3	144.1	.1	B
185	40104	17:36	29.090	58.367	10.09	145	65	30	41.3	63.1	152	272.8	1.2	3.7	38.2	C
187	40104	18:03	29.090	58.369	13.77	230	60	−20	−29.7	72.8	−148	193.5	34.2	97.8	8.3	A
188	40104	18:17	29.089	58.367	13.78	230	60	−20	−29.7	72.8	−148	193.5	34.2	97.8	8.3	A
189	40104	20:56	29.060	58.356	12.39	−15	50	80	180.3	41.0	102	82.1	4.5	202.5	81.1	C
191	40104	21:56	29.070	58.361	12.39	−15	50	80	180.3	41.0	102	194.8	24.3	99.9	10.8	A
192	40104	22:13	29.070	58.354	14.91	140	85	150	232.9	60.1	6	190.3	17.0	92.2	24.6	A
194	40104	22:38	29.031	58.368	16.61	−15	75	−150	246.5	61.1	−17	209.0	31.6	113.3	9.1	B
195	40104	23:14	29.010	58.373	11.04	260	85	−10	−9.1	80.0	−175	215.1	10.8	305.8	3.6	A
197	40104	23:35	29.003	58.372	14.63	140	60	100	−59.4	31.5	73	222.7	14.5	74.9	73.1	A
198	40104	23:39	28.995	58.362	10.98	180	65	120	−53.8	38.3	43	248.5	14.8	132.8	58.6	A
200	50104	01:32	29.091	58.438	20.19	110	30	90	−70.	60.0	90	20.0	15.0	200.0	75.0	B
201	50104	02:34	29.037	58.350	13.61	5	90	−180	−85.	90.0	0	230.0	.7	320.0	.7	A
202	50104	02:50	29.006	58.365	13.79	30	75	−60	144.1	33.2	−152	334.0	50.7	97.2	24.1	B
207	50104	05:54	29.000	58.359	14.40	170	65	150	−86.3	63.1	28	222.2	1.2	131.3	38.2	B
208	50104	06:00	29.078	58.362	11.10	−5	60	−120	224.1	41.4	−49	215.9	62.1	106.0	10.2	C
211	50104	07:30	29.034	58.362	11.69	220	65	−10	−45.7	80.9	−155	179.8	24.3	84.9	10.8	B
214	50104	11:25	29.040	58.369	12.32	−5	35	60	210.2	60.2	109	286.3	13.2	159.8	68.5	B
215	50104	11:40	29.109	58.344	10.23	−65	90	170	25.	80.0	0	160.0	.7	250.0	.7	B
216	50104	11:43	29.060	58.352	10.59	80	65	−20	178.7	71.9	−154	41.0	31.1	308.2	4.6	B
218	50104	16:41	29.109	58.345	11.07	20	90	−30	110.	60.0	−180	335.0	.7	245.0	.7	B
221	50104	17:59	29.014	58.357	13.24	−15	80	−160	251.4	70.3	−11	209.6	21.1	117.0	6.6	B
223	50104	18:35	29.044	58.365	11.13	5	50	−110	214.5	44.0	−68	210.4	74.5	109.0	3.1	C
227	50104	20:23	29.063	58.342	15.46	265	85	0	175.	90.0	175	220.1	3.5	129.9	3.5	A
229	50104	20:58	29.046	58.342	12.68	110	70	10	16.5	80.6	160	64.6	7.2	331.8	21.0	B
230	50104	21:29	29.073	58.357	14.33	75	80	0	−15.	90.0	170	30.4	7.1	299.6	7.1	B
234	50104	23:12	29.112	58.359	12.67	120	60	−140	7.2	56.2	−37	335.4	48.4	242.8	2.3	B
236	50104	23:53	29.051	58.370	11.42	220	55	−50	−15.6	51.1	−133	189.4	58.2	283.0	2.2	C
237	60104	00:38	29.080	58.360	11.63	215	85	170	−54.1	80.0	5	260.8	3.6	170.1	10.8	A
238	60104	01:01	29.081	58.348	13.72	75	60	−70	218.9	35.5	−121	25.8	68.3	150.6	12.8	B
239	60104	01:09	29.105	58.349	13.22	−5	85	−160	263.2	70.1	−5	220.8	17.5	127.5	10.2	A
240	60104	01:44	29.042	58.357	12.99	155	65	140	264.5	54.4	31	211.9	6.5	115.4	45.3	A
244	60104	03:54	29.139	58.400	9.16	25	70	−120	264.4	35.5	−36	257.1	54.8	137.1	19.5	B
247	60104	05:01	29.029	58.351	9.73	95	80	−10	186.8	80.2	−170	50.9	14.3	140.9	.1	A
249	60104	08:22	29.043	58.360	15.02	50	50	−60	188.1	48.4	−121	27.3	67.5	119.3	.8	A
251	60104	08:39	29.058	58.355	14.36	240	85	0	150.	90.0	175	195.1	3.5	104.9	3.5	A
252	60104	09:44	29.037	58.346	12.86	45	75	−30	143.5	61.1	−163	1.0	31.6	96.7	9.1	B
253	60104	10:36	29.057	58.357	12.00	240	80	0	150.	90.0	170	195.4	7.1	104.6	7.1	A
255	60104	11:27	29.128	58.354	12.86	155	50	−150	44.6	67.5	−44	2.2	46.5	103.5	10.6	A
257	60104	13:17	29.041	58.356	12.86	85	90	0	−5.	90.0	180	40.0	.7	310.0	.7	A
258	60104	14:39	29.036	58.346	12.51	85	90	−10	175.	80.0	−180	40.0	.7	310.0	.7	A
260	60104	17:27	29.007	58.365	13.21	70	80	−60	176.7	31.5	−161	27.0	6.1	125.3	53.4	A
261	60104	17:32	29.082	58.359	8.93	135	70	10	41.5	80.6	160	89.6	7.2	356.8	21.0	B
262	60104	17:49	29.059	58.338	12.56	80	80	−60	186.7	31.5	−161	21.0	46.5	146.2	28.7	B
263	60104	18:15	29.047	58.380	13.91	125	60	80	−35.6	31.5	107	222.3	14.5	10.1	73.1	A
264	60104	18:19	29.130	58.337	12.79	110	40	70	−44.6	52.8	106	34.1	6.6	277.3	75.7	B
265	60104	18:27	29.125	58.352	11.42	190	85	−170	99.1	80.0	−5	54.9	10.8	324.2	3.6	A
267	60104	19:39	29.101	58.363	8.72	−80	85	10	189.1	80.0	175	54.2	3.6	144.9	10.8	A
268	60104	20:20	29.075	58.352	13.06	55	75	−40	157.3	51.6	−161	8.7	38.5	111.0	14.9	A
269	60104	20:57	29.041	58.407	11.60	210	65	170	−55.7	80.9	25	74.9	10.8	169.8	24.3	B
270	60104	21:31	29.079	58.383	15.50	5	90	170	95.	80.0	0	230.0	.7	320.0	.7	A
271	60104	21:33	29.120	58.337	9.71	145	65	120	−88.8	38.3	43	213.5	14.8	97.8	58.6	B
273	60104	23:04	29.012	58.359	11.64	155	55	−180	65.	90.0	−35	14.3	23.9	115.7	23.9	A
275	60104	23:37	29.107	58.342	12.98	−25	80	−160	241.4	70.3	−11	199.6	21.1	107.0	6.6	B
276	70104	00:23	29.037	58.362	13.65	265	85	10	174.1	80.0	175	39.2	3.6	129.9	10.8	A

Downloaded from https://academic.oup.com/gji/article/163/1/90/739453 by guest on 19 February 2021

Table 2. (*Continued.*)

Nb	Date	Time	Lat	Lon	Depth	Az1	Pl1	de1	Az2	Pl2	de2	Azp	dep	Azt	det	Q
277	70104	00:24	29.093	58.348	11.29	260	85	10	169.1	80.0	175	34.2	3.6	124.9	10.8	A
278	70104	00:29	29.026	58.364	11.66	225	85	0	135.	90.0	175	180.1	3.5	89.9	3.5	B
279	70104	01:36	29.015	58.356	13.35	5	35	80	197.1	55.6	97	282.1	10.4	131.6	78.2	B
280	70104	03:25	29.091	58.366	9.30	45	80	160	138.6	70.3	11	93.0	6.6	.4	21.1	C
282	70104	04:27	29.049	58.360	11.01	185	85	−180	95.	90.0	−5	49.9	3.5	140.1	3.5	A
284	70104	04:55	29.008	58.344	16.87	160	80	170	251.8	80.2	10	205.9	.1	115.9	14.3	A
285	70104	06:24	29.052	58.360	12.16	30	90	10	−60.	80.0	180	345.0	.7	255.0	.7	A
286	70104	11:16	29.145	58.335	9.42	−30	85	−150	237.1	60.1	−6	197.8	24.6	99.7	17.0	B
287	70104	11:56	29.081	58.357	10.67	75	75	−10	167.6	80.3	−165	31.9	17.5	300.7	3.7	A
288	70104	12:07	29.052	58.361	12.38	205	85	20	113.2	70.1	175	337.5	10.2	70.8	17.5	B
289	70104	13:45	29.010	58.360	9.02	20	80	−160	−73.6	70.3	−11	244.6	21.1	152.0	6.6	B
290	70104	15:30	29.108	58.347	11.34	−40	85	−150	227.1	60.1	−6	187.8	24.6	89.7	17.0	B
292	70104	17:01	29.097	58.367	10.37	25	90	−180	−65.	90.0	0	250.0	.7	340.0	.7	A
296	70104	18:32	28.996	58.361	10.66	185	70	150	−73.8	62.0	23	237.1	5.2	143.4	35.1	B
297	70104	19:32	29.088	58.348	14.27	85	90	−10	175.	80.0	−180	40.0	.7	310.0	.7	A
298	70104	20:30	29.073	58.356	13.81	240	70	0	150.	90.0	160	196.8	14.0	103.2	14.0	A
301	80104	06:43	29.038	58.364	10.89	−85	85	10	184.1	80.0	175	49.2	3.6	139.9	10.8	A
302	80104	07:43	29.021	58.365	15.54	85	80	−10	176.8	80.2	−170	40.9	14.3	130.9	.1	A
306	90104	07:18	29.006	58.360	10.01	260	80	−10	−8.2	80.2	−170	215.9	14.3	305.9	.1	A
308	90104	11:28	29.024	58.360	10.94	65	35	−120	−79.8	60.2	−71	229.8	68.5	356.3	13.2	B
309	90104	14:29	29.046	58.359	7.85	−85	80	−10	6.8	80.2	−170	230.9	14.3	320.9	.1	A
310	90104	16:29	29.097	58.353	11.43	−20	70	−150	238.8	62.0	−23	201.6	35.1	107.9	5.2	B
312	90104	18:33	29.101	58.340	11.05	−25	75	−150	236.5	61.1	−17	199.0	31.6	103.3	9.1	B
313	90104	18:49	29.080	58.359	13.81	260	80	0	170.	90.0	170	215.4	7.1	124.6	7.1	A
316	100104	10:38	29.069	58.351	16.28	65	75	−20	160.4	70.7	−164	22.0	24.7	113.3	2.9	A
318	110104	07:08	29.047	58.394	9.92	−60	85	40	205.8	50.2	173	66.0	23.1	170.9	31.0	B
320	110104	10:52	29.043	58.354	8.91	35	50	−60	173.1	48.4	−121	12.3	67.5	104.3	.8	C
324	140104	09:36	29.122	58.330	10.48	125	70	160	222.1	71.3	21	353.4	.8	83.8	28.0	A
327	160104	06:55	29.042	58.354	11.69	170	30	140	−64.	71.3	66	44.1	22.7	174.2	57.1	B
328	160104	12:41	29.106	58.344	6.69	100	60	10	5.	81.4	150	56.0	14.4	318.4	27.3	A
329	170104	12:03	29.060	58.361	6.39	0	80	−130	258.3	41.0	−15	233.0	41.0	119.9	24.3	A
330	170104	13:22	29.036	58.358	13.50	95	70	0	5.	90.0	160	51.8	14.0	318.2	14.0	A

Lat, Lon, Depth are the coordinates of the aftershocks, Az1, Pl1, de1, AZ2, Pl2, de2 are Azimuth, dip and slip of plane 1 and 2, respectively. Azp, dep, Azt, det are azimuth and dip of *P*- and *T*-axis, respectively. A, B and C are a factor of quality of the fault plane solutions.

berg & Oppenheimer 1985) to compute the nodal planes and we keep only the 161 solutions that show no inconsistent polarities. We take into consideration the quality of the azimuthal coverage on the focal sphere and the possibility of alternative solutions in order to distribute the solutions into three categories depending on their reliability. We put the mechanisms for which four quadrants are sampled and the two planes are constrained within 20° in category A. In category B, only three quadrants are sampled and the two planes are well constrained. In category C, only two quadrants are sampled, or alternative solutions are possible.

AFTERSHOCK DISTRIBUTION AND FOCAL MECHANISMS

Firstly we locate again all the 544 events recorded by a minimum of 8 *P* and 5 *S* arrival times with the appropriate velocity structure (Table 1). The resulting map (Fig. 4) shows that the aftershocks define a N–S trending cluster approximately 25 km long and 7 km wide. The depth of the seismicity ranges from 6 km to 20 km (Fig. 5). This aftershock distribution is consistent with a N–S trending active fault, as inferred from waveforms and InSAR observations (Talebian *et al.* 2004; Funning *et al.* 2005). It is definitely located ∼10 km east of the relocated EHB main aftershocks (Engdahl, personal communication) and west of the Bam-Baravat escarpment. On the other hand, it is located right beneath the co-seismic surface fissures observed south of Bam after the main shock by Talebian *et al.* (2004). Thus, there is a systematic bias, probably due to an uncertain velocity structure, in the teleseismic earthquake locations in this area. A section across the seismicity (Fig. 5) shows a cluster dipping almost vertically from 6 to 18 km that is not obviously connected at the surface to the Bam-Baravat escarpment or to the co-seismic breaks.

In order to ensure our interpretation of the aftershock seismicity and of the related active fault, we plot the 331 selected events that are more precisely located since they fulfil quality criteria. These criteria do not prevent from systematic bias, but because our network closely surrounds the epicentral area, we are confident that such bias should be small. Again, the seismicity (Fig. 6) is centred on 29.10 °N latitude and 58.37 °E longitude exactly beneath the city of Bam and is elongated in a N–S direction which confirms an active fault trending N–S. It is approximately 20 km long and, therefore, longer than the observed co-seismic surface ruptures. We observe (Fig. 6) that the cluster of seismicity is narrower in its southern part of the cluster than in its northern part where it spreads slightly. For this reason, and to refine our previous cross-section, we computed three sections, 8 km wide, across the aftershock seismicity (Fig. 7). Indeed, the southernmost section CC′ better defines a vertical plane but it is still problematic to relate the fault plane at the surface, either to the Bam-Baravat escarpment or to the co-seismic surface breaks. The shallowest part (6–14 km deep) seems to dip steeply with an angle of ∼80° westward, contrary to what is suggested by

Downloaded from https://academic.oup.com/gji/article/163/1/90/739453 by guest on 19 February 2021

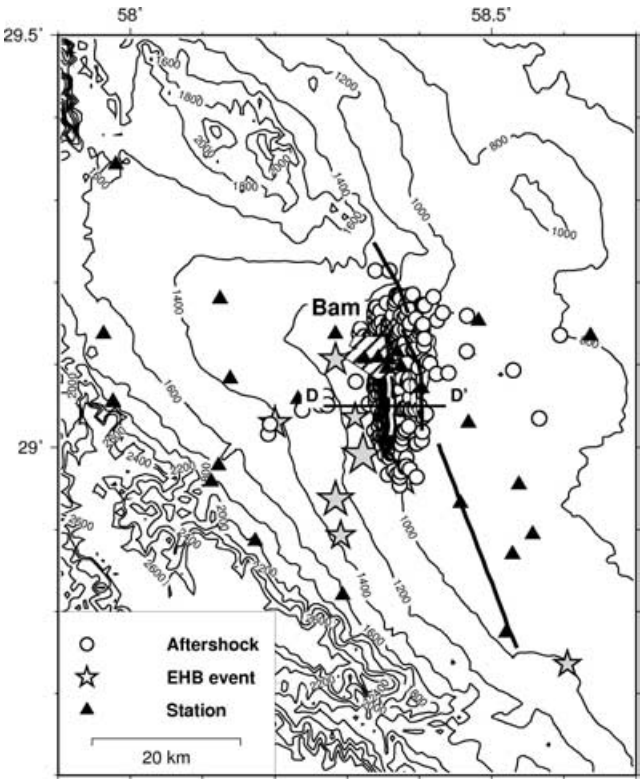

Figure 4. Seismicity map of all 544 aftershocks recorded by more than eight stations, with a minimum of eight *P* and five *S* arrival times. The triangles are the seismological stations. The stars are the EHB teleseismically relocated main aftershocks (Engdahl, personal communication). The Bam-Baravat escarpment fault is plotted in black and the co-seismic cracks in white (Talebian *et al.* 2004).

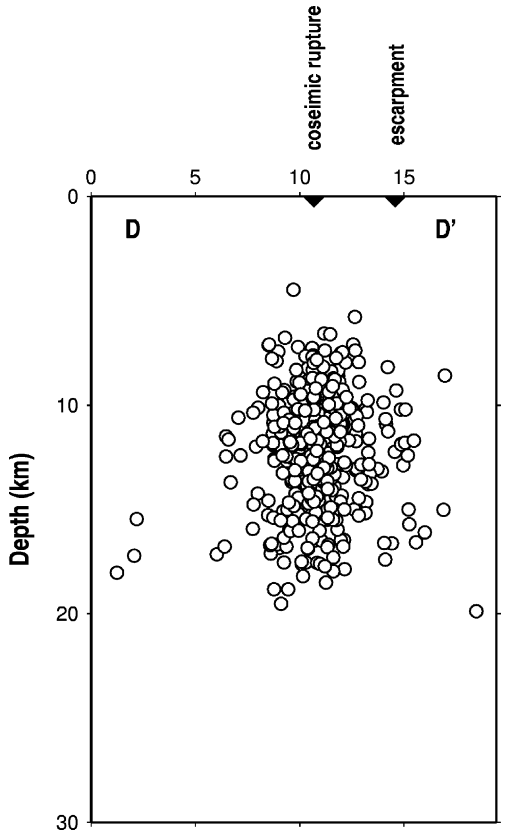

Figure 5. EW trending section across the 544 aftershocks showing an almost vertical plane located beneath the co-seismic surface cracks. We report the trace at the surface of the Bam-Baravat escarpment and of the co-seismic surface breaks. Aftershocks are concentrated between 6- and 20-km depth, deeper than the centroid depth of the main shock.

body-wave modelling (Talebian *et al.* 2004) or InSAR imagery (Wang *et al.* 2004).

In order to eliminate any scatter due to local heterogeneity in the velocity structure and refine our interpretation, we relocate the earthquakes previously located independently, using the double difference method HypoDD (Waldhauser & Ellsworth 2000). If the hypocentral distance between events is small compared to the distance to the stations, the effects of anomalies on the ray path are minimized by HypoDD because it locates events relative to each other within clusters. This method is particularly useful to map clusters of earthquakes and infer possible active faults. We choose to have pairs with a minimum of 12 links (traveltimes to stations) and distances between events belonging to the same pair smaller than 20 km. Because our seismicity is clustered we remain with one cluster of 286 events (Fig. 8). The seismicity is slightly better defined after relocating with the HypoDD technique. The southernmost part is narrower than the northernmost part. Fig. 9 shows three sections trending E–W perpendicular to the distribution of aftershocks. The southernmost sections strongly suggest that the fault plane is dipping westward with an angle of about 80°. The organized part of the middle section confirms this westward dip. The northernmost section is more scattered. All events concentrate between 8- and 18-km depth (Fig. 10), significantly deeper than the centroid depth computed by body-wave modelling (Talebian *et al.* 2004) and deeper than the extent of rupture inferred from InSAR (Funning *et al.* 2005).

We plot with different symbols the two classes of focal mechanisms A and B (Fig. 11). Most of the reliable solutions (category A) show right-lateral strike-slip motion on a N–S trending fault plane. In a few cases, we observe either reverse mechanisms, trending NW–SE, or normal faulting trending the opposite. These solutions are never of category A (because in this case we cannot sample four quadrants) and are often associated with other possible solutions with the same readings. A section of the focal mechanisms (Fig. 12) confirms that most of the fault planes dip consistently slightly westward as suggested by the seismicity distribution. In order to get an estimate of the state of strain along the fault, we also plot the direction of the *P*-axes (Fig. 13). They are consistently trending NE–SW and do not display any obvious rotation.

DISCUSSION

The damage due to the Bam earthquake was larger than expected from such a moderate magnitude event, raising several questions on the characteristics of the main shock rupture. We discuss here the contribution of the aftershock study to a better understanding of the main shock. Aftershocks are usually located in places of increased stress (i.e. Das & Henry 2003). This could be on local heterogeneities of the main fault (helping to map the active fault), or at the end of the fault, or off the fault where the Coulomb failure criteria is reached. Local heterogeneities on the main fault are usually related to barriers and asperities of various size. As an example, a region of large slip gradient is related to an asperity and usually associated with aftershocks located on planes favourably oriented. Usually, aftershocks expand rapidly in time, the early aftershocks being located close to the main active fault whereas they could spread in a larger volume

Downloaded from https://academic.oup.com/gji/article/163/1/90/739453 by guest on 19 February 2021

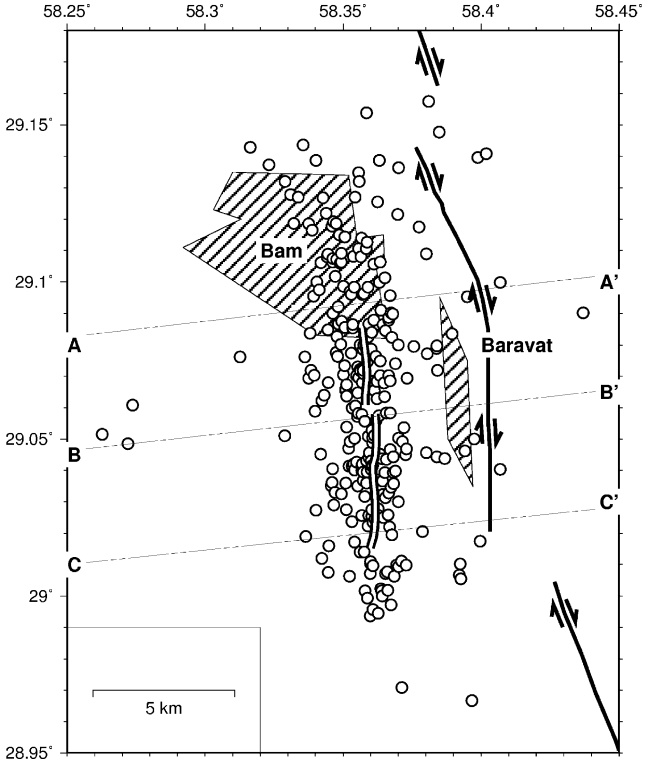

Figure 6. Selected seismicity of the 331 earthquakes located with a rms less than 0.1 s, and uncertainties in location less than 1 km in more than 10 stations. Symbols as in Fig. 4.

after a few days. Therefore, the information provided by aftershocks is different and complementary to information provided by geodesy and tectonics. Aftershocks help map the active fault, but because they are restricted to the region of stress increase and not to large slip, they should not necessarily give the same picture.

LOCATION OF THE MAIN SHOCK

The first question is related to the location of the main shock relative to the Bam fault and to the city of Bam. Our aftershock seismicity is definitely located 10 km east of the teleseismically relocated main shock and 5 km west of the Bam-Baravat escarpment. It is located exactly beneath the city of Bam which could explain the heavy damage in the city, and beneath the surface ruptures (Talebian *et al.* 2004; Wang *et al.* 2004; Funning *et al.* 2005). The aftershock seismicity is deeper than 7 km (and therefore deeper than the centroid depth of the main shock).

CHARACTERISTICS OF THE MAIN SHOCK

The length of the aftershock seismicity is approximately 18 km, the depth range is about 15 km, leading to a minimum fault surface of 270 km^2. Assuming a shear modulus of 3×10^{11} dyne cm^{-2}, a moment M0 of 9.3 10^{25} dyne cm gives us an upper bound of 110 cm for the mean slip on the fault (assuming that the fault is restricted to the aftershock region). This is twice more than the empirical relationship given by Wells & Coppersmith (1994) but less than the peak slip of 2.7 m locally inferred from InSAR imagery although

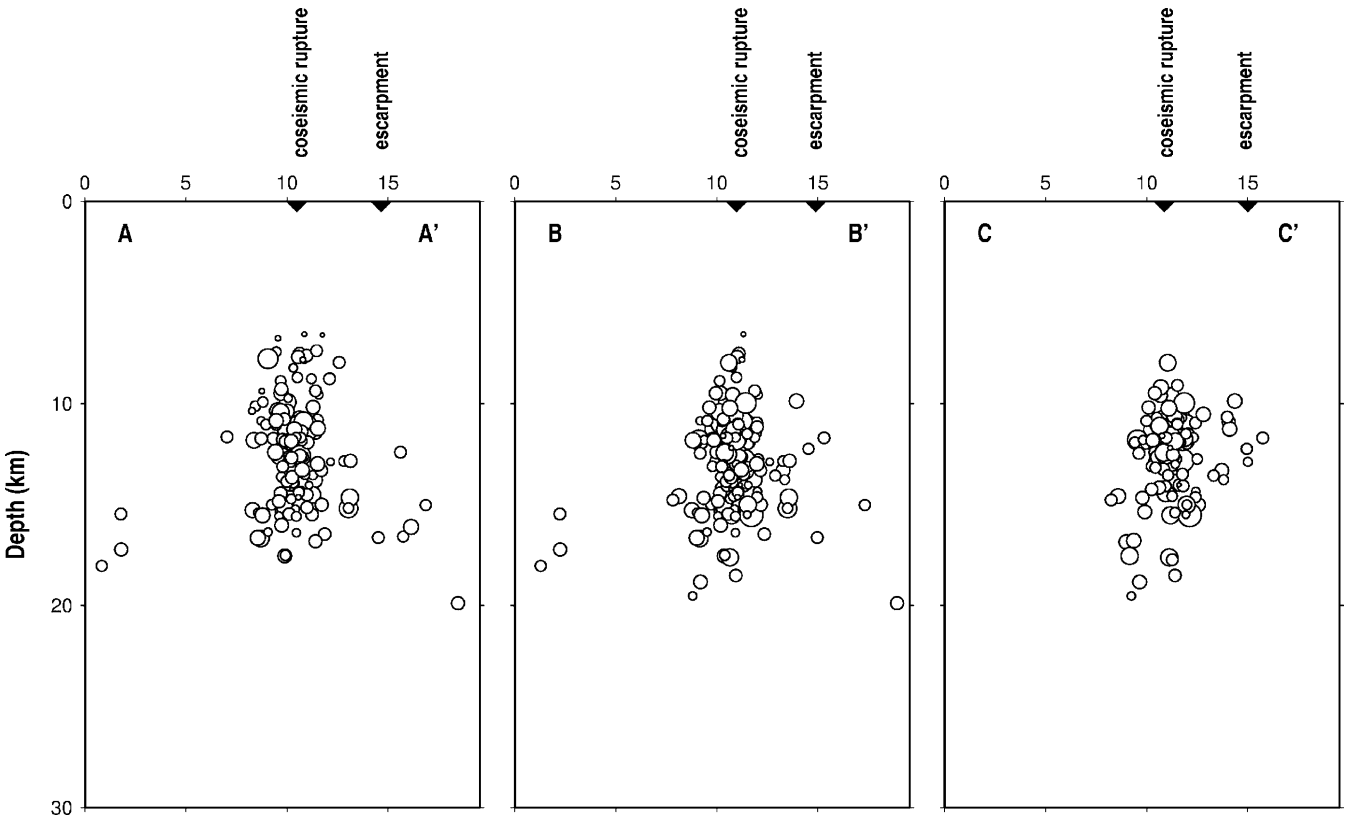

Figure 7. EW trending section across the 331 selected earthquakes at three different places (see Fig. 6). The southern B–B′ and C–C′ sections suggest a westward dipping plane especially at shallow depth.

Downloaded from https://academic.oup.com/gji/article/163/1/90/739453 by guest on 19 February 2021

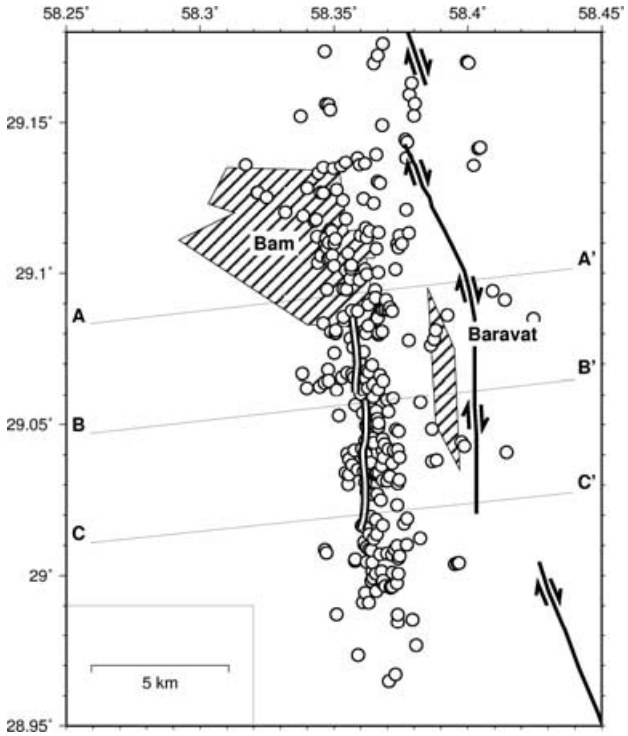

Figure 8. Seismicity map of the 286 relocated aftershocks using the Double Difference method (Waldhauser & Ellsworth 2000). The distribution of the relocated events shows a slightly better defined zone in the southern part of the fault.

it is comparable to the mean slip (∼1.5 m) averaged on the fault (Funning *et al.* 2005).

EXISTENCE OF ONE OR TWO ACTIVE FAULTS

The relation of the active fault plane to the surface features is still a matter of debate. Some authors (Hessami *et al.* 2004; Fu *et al.* 2004) suggest that the Bam-Baravat escarpment is the only active fault. Other authors (Talebian *et al.* 2004; Funning *et al.* 2005) suggest that co-seismic slip occurred on 2 different faults, a vertical strike-slip fault located west, beneath the co-seismic surface breaks, and a reverse fault dipping 60° westward that reaches the surface 5 km to the east, beneath the Bam-Baravat escarpment. Wang *et al.* (2004) suggest that a single fault, located beneath the co-seismic surface ruptures was active. We believe that our HypoDD relocated aftershocks are better located than 2 km in any case (we selected only events with ERH and ERZ better than 1 km and with 12 readings and we conducted several tests that do not shift the hypocenters more than 1 km). We observe a single cluster located right beneath the city of Bam. There is no aftershock seismicity that could be related to a west-dipping secondary reverse fault located further east. However, since this fault is supposed to be active only in its deepest part (Fielding *et al.* 2005), it would be difficult to detect. Most of the mechanisms are strike-slip motions, consistently striking N–S along the fault and only a very few reverse mechanisms are observed. In summary, aftershocks do not support the evidence of two distinct faults.

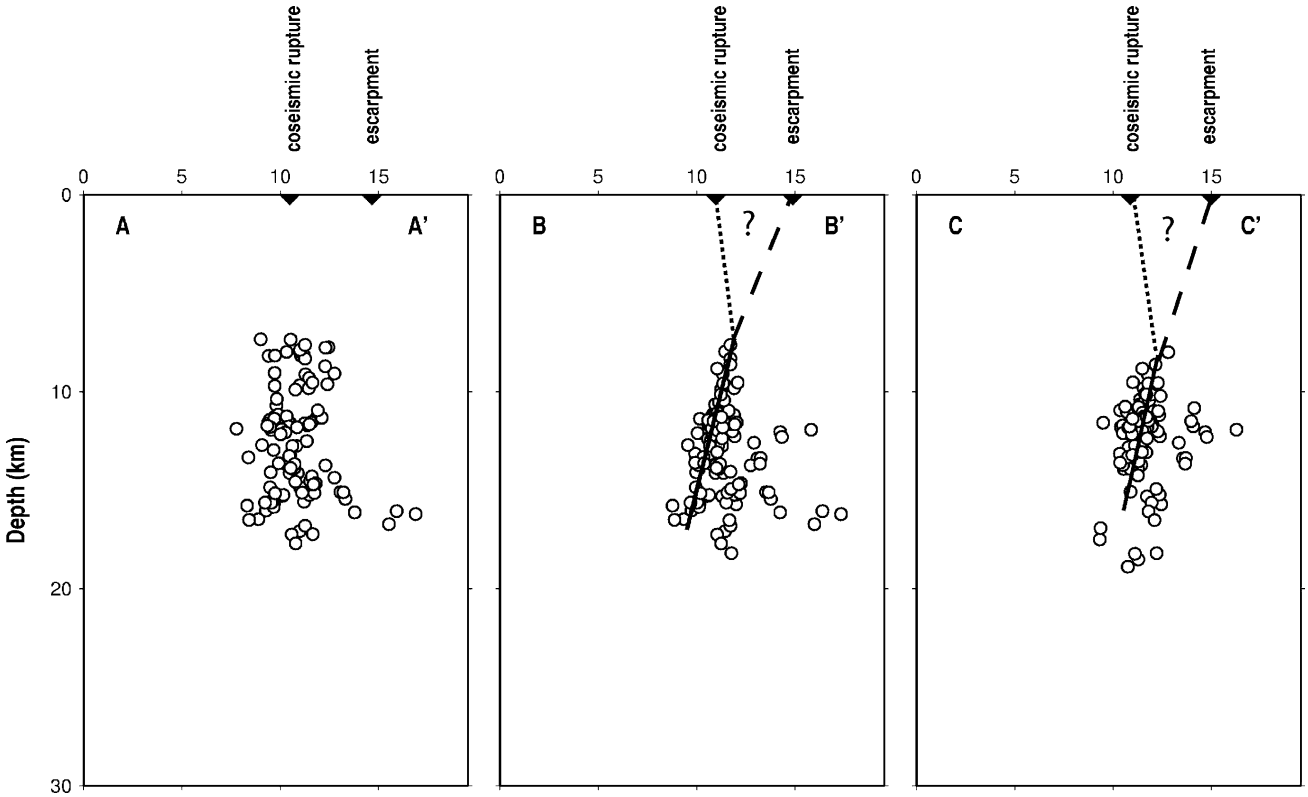

Figure 9. EW trending sections across the relocated events by Double Difference (Waldhauser & Ellsworth 2000). Symbols as for Fig. 5. Again the southern sections (B–B′ and C–C′) suggest a slightly westward dipping plane (underlined by the heavy line) contrary to body-wave modelling (Talebian *et al.* 2004), or InSAR determination (Wang *et al.* 2004). This line stops at 8-km depth, which is the lower boundary of the 5.3 km s^{-1} layer. The fault connects at surface to the co-seismic ruptures (dotted line) or to the Bam-Baravat escarpment (dashed line).

Downloaded from https://academic.oup.com/gji/article/163/1/90/739453 by guest on 19 February 2021

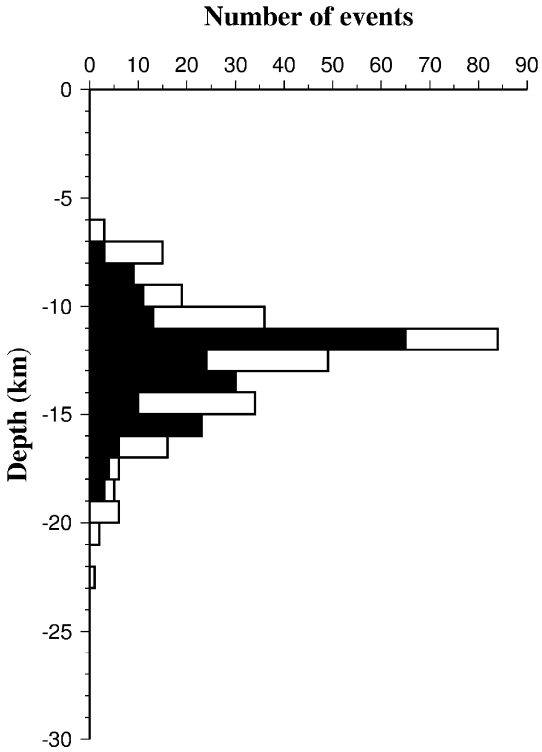

Figure 10. Depth distribution of the aftershocks. White is for the 331 selected aftershocks. Black is for the 286 HypoDD relocated aftershocks. There is no seismic activity shallower than 5 km.

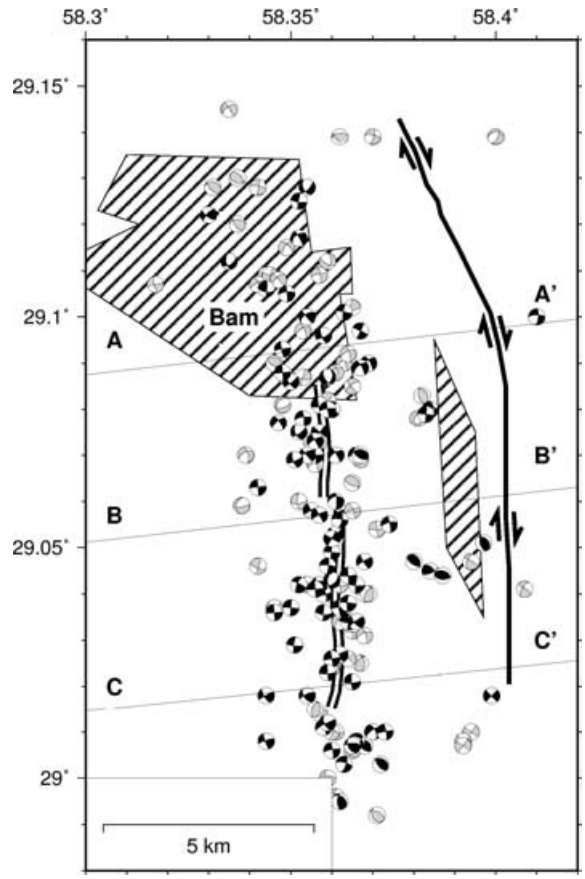

Figure 11. Map of the focal mechanisms for aftershocks located better than 1 km (horizontally and vertically) with HYPO71 and a minimum of 12 first motion polarities. The calculated focal mechanisms are divided into two groups based on their quality (see text): A (Black), B (dark grey).

FAULT COMPLEXITY

The relative locations of the aftershocks (Fig. 8) define a narrower zone in the South than in the North. It is also consistent with the wider area of surface disruptions mapped by Fielding *et al.* (2005). If we assume, as suggested by the teleseismic body-wave modelling (Talebian *et al.* 2004), that the rupture propagated northward along the fault, then the width of the fault zone progressively spread as it propagated. This increasing complexity of the fault zone, from the initiation to the termination along the fault, has been observed in other aftershock studies in El-Asnam, Algeria in 1980 (Ouyed *et al.* 1983) or in Kozani, Greece in 1995 (Hatzfeld *et al.* 1997). This complexity is also observed in the focal mechanisms and suggests that the northward termination of the seismic rupture is likely to be associated with spreading into several branches.

RELATIONSHIP WITH SURFACE FEATURES

The aftershock seismicity is deeper than 6 km. In the southern part of the cluster, it defines a very narrow fault zone dipping slightly westward with an angle of about 75°. This is especially clear on the HypoDD relocated events (Figs 9b and c). On the other hand, the shallowest events (at 6-km depth) are located exactly beneath the surface breaks. The prolongation to the surface of the best-located events of the southern segment C–C′ is located 3 km east of the co-seismic surface breaks and 2 km west of the Bam-Baravat escarpment. It could fit either the Bam-Baravat escarpment or the co-seismic surface breaks (Fig. 9c). This peculiar observation of aftershocks located on an active fault that does not reach the surface but produces breaks vertically above the termination of the rupture has been made in other aftershock studies such as Kozani in Greece in 1995 (Hatzfeld *et al.* 1997). The shallowest events are deeper than the interface between a 6.0 km s^{-1} and 5.3 km s^{-1} layers. Relying on all these observations, we think that, (1) at depth, within the rheologically hard layer, the rupture was located on the Bam-Baravat fault as evidenced by aftershock seismicity, but (2) at surface, because of the soft layer, the main rupture branched to the surface ruptures, as evidenced by InSAR imagery.

RELATIONSHIP BETWEEN AFTERSHOCKS AND THE INSAR INFERRED FAULT

At depth, the aftershocks are restricted between 8 and 16 km within the 6.0 km s^{-1} layer (Fig. 10). This is deeper than the 6-km depth inferred from body-wave modelling of the main shock centroid (Talebian *et al.* 2004). It is also deeper than the area of important slip inferred from InSAR measurements of 3–8 km by Funning *et al.* (2005) or 2–5 km Wang *et al.* (2004). We are confident that our depths cannot be shallower than 5 km (Fig. 14), because several tests showed that

(1) a slightly slower velocity structure does not change the hypocentral depths significantly and

(2) there is no bias due to the velocity interface within the crust as shown by a computation in an half space model.

Downloaded from https://academic.oup.com/gji/article/163/1/90/739453 by guest on 19 February 2021

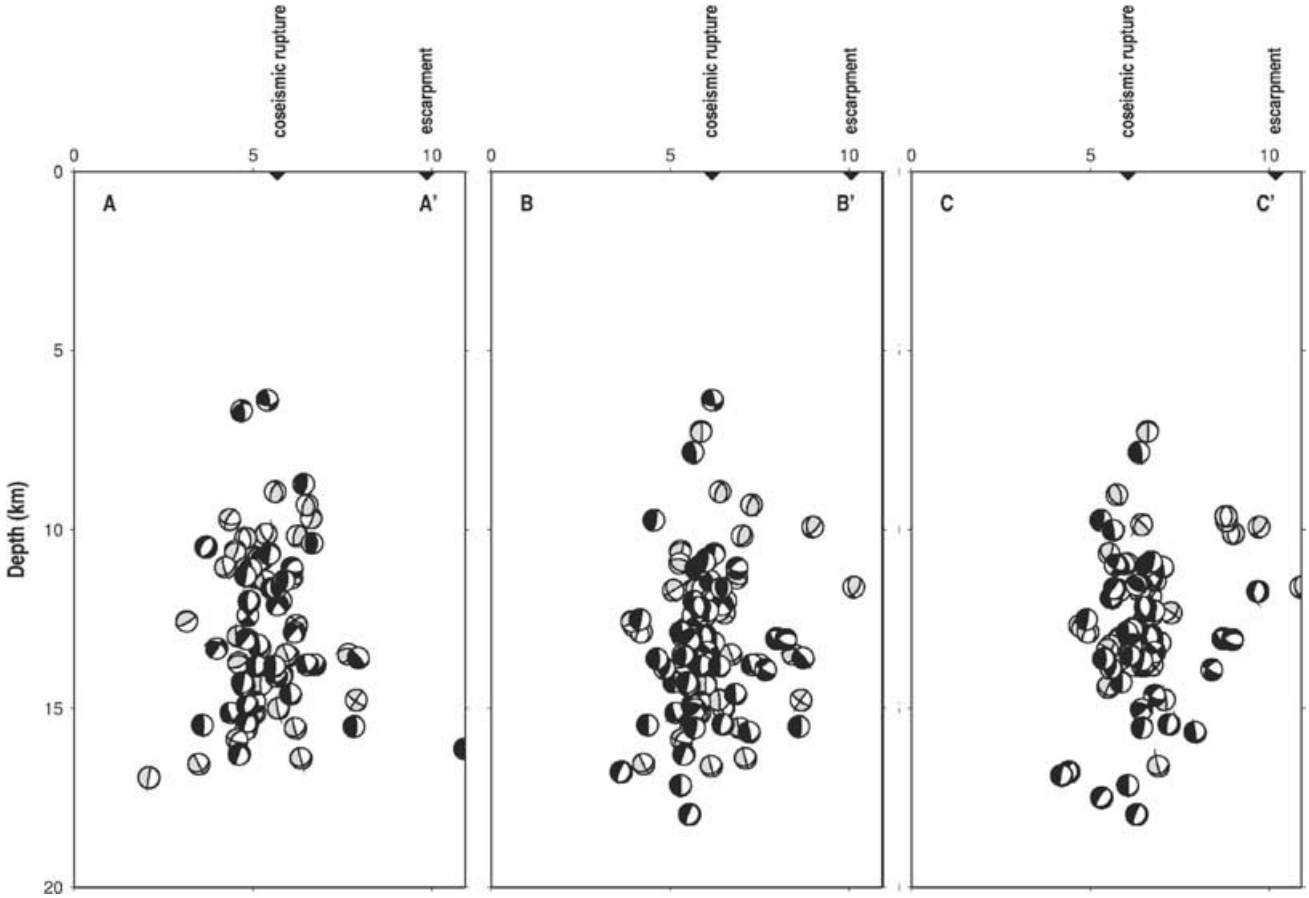

Figure 12. Cross-section of focal mechanisms of category A and B (see text). The mechanisms are projected on the back plane. We observe that several mechanisms have one plane dipping westward almost vertically as suggested by the seismicity.

The shallow depth inferred from InSAR observations is also well constrained by the wavelength of the interferograms. However, there are two possible uncertainties in the InSAR results. One is the effect of a shallow layer of different Young modulus that would induce a bias of 1–2 km in depth and 40 per cent in slip as for normal faulting (i.e. Cattin *et al.* 1999; Amoruso *et al.* 2004). The second is that the resolution on the displacement decreases significantly with depth and is usually poor beneath 8–10 km (i.e. Hernandez *et al.* 1999; Loevenbruck *et al.* 2004). Therefore, the difference in depth between the slip area and the aftershocks could be smaller than the observed one.

Usually, such a shift between the area of important slip and aftershocks is attributed to stresses relaxed during the main shock (i.e. Mendoza & Hartzell 1988). In the case of the Bam earthquake, we do not observe specific patches free of earthquakes, but a systematic shift between aftershocks and slip. This systematic shift between aftershock seismicity and fault slip has also been observed for other events such as the 2000 Tottori earthquake in Japan (Semnane *et al.* 2005). It has been attributed to a large and elongated asperity located at shallow depth that was associated with an important slip. Such an asperity associated with a strong slip gradient would produce an unusually large ground motion responsible for large damage (Bommer *et al.* 2004).

CONCLUSION

Aftershock seismicity likely to occurs in areas of local heterogeneities of slip on the active fault plane. For the Bam earthquake, it defines a single plane, slightly dipping westward and located between the co-seismic surface breaks and the Bam-Baravat escarpment. Because aftershocks are deeper than 6 km, any small change in the dip of the fault could connect the active plane either to the co-seismic breaks or to the Bam-Baravat escarpment itself. For simplicity, and because we do not understand how two faults with different dips, orientations, and types could be located so close to each other in a simple stress pattern, we favour the hypothesis that the active fault was at depth the Bam-Baravat escarpment and it did not break at the surface. Moreover, we suggest that the fault rupture started at depth on the Bam-Baravat fault and branched more vertically segment within the shallow layer of 5.3 km s^{-1} to reach the surface at the surface breaks. We also favour the hypothesis of strong earthquakes occurring on weak pre-existing faults rather than initiating new faults. The area of maximum slip estimated from InSAR modelling is systematically shallower than the aftershocks but it did not break the surface either. Such a strong slip gradient at shallow depth could explain the large ground amplification responsible for important damage.

ACKNOWLEDGMENTS

This work was supported by IIEES and LGIT. DH and AP were supported by Insu-CNRS. We thank M. Ghafory-Ashtiany and M. Mokhtari for their help and support during the field experiment. We benefited of interesting discussion with J. Jackson and E. Fielding. We are grateful to H. Grosser and B. Parsons for helpful reviews.

Downloaded from https://academic.oup.com/gji/article/163/1/90/739453 by guest on 19 February 2021

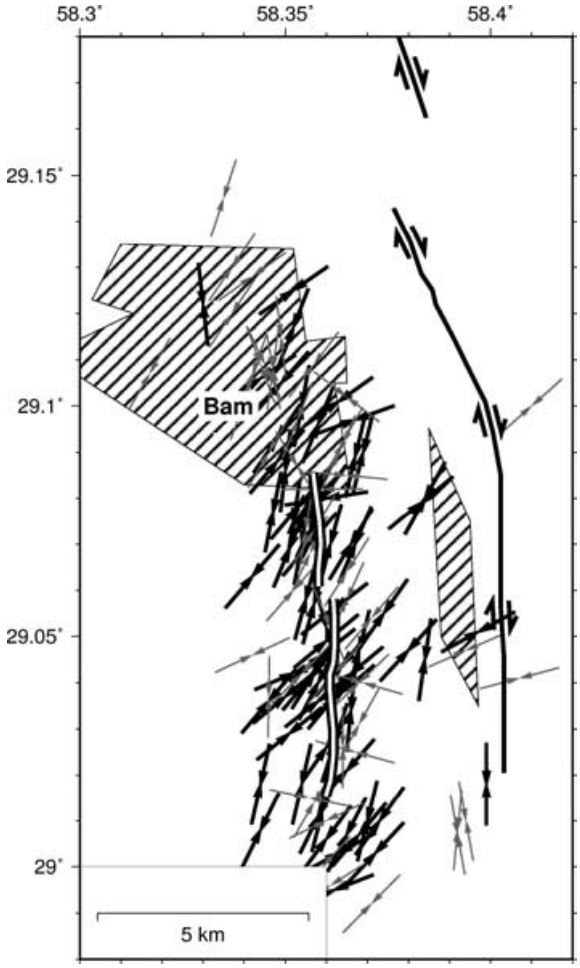

Figure 13. Horizontal projection of the *P*-axes (dipping less than 45°) associated with the focal mechanisms. Thick arrows are for category A mechanisms, while thin arrows are for category B (see text).

The seismological network was composed partially of Lithoscope instruments. We thank all observers and drivers who helped in the field.

REFERENCES

Ambraseys, N. & Melville, C., 1982. *A history of Persian Earthquakes*, Cambridge Univ. Press, Cambridge, UK.

Amoruso, A., Crescentini, L. & Fidani, C., 2004. Effects of crustal layering on source parameter inversion from coseismic geodetic data, *Geophys. J. Int.,* **159,** 353–364.

Berberian, M., 1976. *Contribution to the Seismotectonics of Iran (partII),* p. 518, Geological Survey of Iran, Tehran.

Berberian, M. & Qorashi, M., 1994. Coseismic fault-related folding during the South Golbaf earthquake of November 20, 1989, in southeast Iran, *Geology,* **22,** 531–534.

Berberian, M. & Yeats, R.S., 1999. Pattern of historical earthquake rupture in the Iranian Plateau. *Bull. seism. Soc. Am.,* **89,** 120–139.

Berberian, M., Jackson, J.A., Ghorashi, M. & Kadjar, M.H., 1984. Field and teleseismic observation of the 1981 Golbaf-Sirch earthquakes in SE Iran. *Geophys. J. R. astr. Soc.,* **77,** 809–838.

Berberian, M. *et al.*, 2001. The March 14 1998 Fandoqa earthquake ($Mw = 6.5$) in Kerman province, SE Iran: re-rupture of the 1981 Sirch earthquake fault, triggering of slip on adjacent thrusts, and the active tectonics of the Gowk fault zone. *Geophys. J. Int.,* **146,** 371–398.

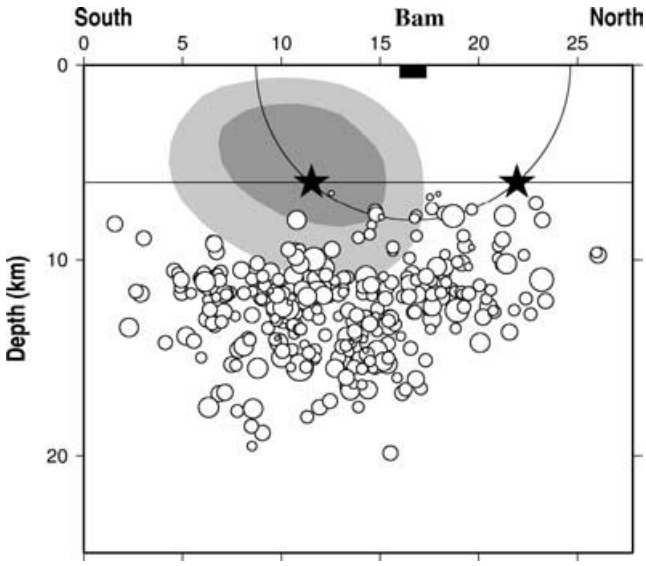

Figure 14. Longitudinal cross-section along the fault. We represent the 331 selected aftershocks and the InSAR inferred co-seismic slip (Funning *et al.* 2005). In dark grey is the area with slip larger than 2 m, in light grey the area with slip was larger than 1 m. We also represent the location of the rupture initiation deduced from the *S–P* arrival time on the strong-motion record in Bam (BHRC, Iran, http://www.bhrc.gov.ir) as a circle (radius = 8 km) centred on Bam and the centroid depth deduced from body-wave modelling (Talebian *et al.* 2004), as a horizontal line at 6-km depth. The star is the intersection of the depth deduced from the centroid and the circle deduced from *S–P* time and the most probable location of the main shock located in the centre of the slip zone above the aftershock seismicity.

Bommer, J.L. *et al.*, 2004. The challenge of Defining Upper Bounds on Earthquake Ground Motions, *Seis. Res. Lett.,* **75,** 82–95.

Cattin, R., Briole, P., Lyon-Caen, H., Bernard, P. & Pinettes, P., 1999. Effects of superficial layers on coseismic displacements for a dip-slip fault and geophysical implications, *Geophys. J. Int.,* **137,** 149–158.

Das, S. & Henry, C., 2003. Spatial relation between main earthquake slip and its aftershock distribution, *Rev. Geophys.,* **41,** 3/1–3/23.

Engdahl, E.R., Van der Hilst, R.D. & Buland, R.P., 1998. Global teleseismic earthquake relocation with improved travel times and procedures for depth determination, *Bull. seism. Soc. Am.,* **88,** 722–743.

Fielding, E.J., Talebian, M., Rosen, P.A., Nazari, H., Jackson, J. A., Ghoraishi, M. & Berberian, M., 2005. Surface ruptures and building damage of the 2003 Bam, Iran earthquake mapped by satellite SAR interferometric correlation, *J. geophys. Res.,* **110,** B03302, doi:10.1029/2004JB003299.

Fu, B., Ninnomiya, Y., Lei, X., Toda, S. & Awata, Y., 2004. Mapping active fault associated with the 2003 Mw 6.6 Bam (SE Iran) earthquake with ASTER 3-D images, *Remote Sensing Environment,* **92,** 153–157.

Funning, G.J., Parsons, B., Wright, T.J., Fielding, E.J. & Jackson, J.A., 2005. Surface displacements and source parameters of the 2003 Bam (Iran) earthquake from Envisat ASAR imagery, *J. geophys. Res.,* in press.

Hatzfeld, D. *et al.*, 1997. The Kozani-Grevena earthquake of May 13, 1995. A seismological study. *Bull. seism. Soc. Am.,* **87,** 463–473.

Hernandez, B., Cotton, F. & Campillo, M., 1999. Contribution of radar interferometry to a two-step inversion of the kinematic process of the 1992 Landers earthquake, *J. geophys. Res.,* **104,** 13 083–13 100.

Hessami, K., Tabassi, H., Abbassi, M.R., Azuma, T., Okumura, K., Echigo, T. & Kondo, H., 2004. Surface expression of the Bam Fault Zone in Southeastern Iran: Causative Fault of the 26 December 2003 Bam Earthquake, *J. Seismology and Earthquake Engineering,* **4,** 5–14.

Jackson, J.A. & McKenzie, D., 1984. Active tectonics of the Alpine-Himalayan Belt between western Turkey and Pakistan, *Geophys. J. R. astr. Soc.,* **77,** 185–264.

Downloaded from https://academic.oup.com/gji/article/163/1/90/739453 by guest on 19 February 2021

Kissling, E., 1988. Geotomography with local earthquake data, *Rev. Geophys.,* **26,** 659–698.

Lee, W.H.K. & Lahr, J.C., 1972. HYPO71 (revised), a computer program for determining hypocenters, magnitude and first motion pattern of local earthquakes, *U.S. Geol. Surv,* Open File Rep., 75–311.

Loevenbruck, A., Cattin, R., Le Pichon, X., Dominguez, S. & Michel, R., 2004. Coseismic slip resolution and post-seismic relaxation time of the 1999 Chi-Chi, Taiwan, earthquake as constrained by geological observations, geodetic measurements and seismicity, *Geophys. J. Int.,* **158,** 310–326.

Mendoza, C. & Hartzell, S.H., 1988. Aftershock patterns and main shock faulting, *Bull. seism. Soc. Am.,* **78,** 1438–1449.

Ouyed, M., Yielding, G., Hatzfeld, D. & King, G.C.P., 1983. An aftershock study of the El Asnam (Algeria) earthquake of 1980 October 10, *Geophys. J. R. astr. Soc.,* **73,** 605–639.

Reasenberg, P.A. & Oppenheimer, D., 1985. FPFIT, FPPLOT and FPPAGE, Fortran computer programs for calculating and displaying earthquake fault-plane solutions, *USGS Open-File Report,* no 85–739.

Semnane, F., Cotton, F. & Campillo, M., 2005. The 2000 Tottori Earthquake: a shallow earthquake with no surface rupture and slip properties controlled by depth, *J. geophys. Res.,* in press.

Talebian, M. *et al.*, 2004. The 2003 Bam (Iran) earthquake- rupture of 'truly blind' fault, *Geophys. Res. Lett.,* **31,** L11, 611, doi:10.1029/2004GL020, 058.

Tatar, M., Hatzfeld, D., Moradi, A.S., Paul, A., Farahbod, A.M. & Mokhtari, M., 2004. Aftershocks study of the 26 December 2003 Bam Earthquake, *JSEE* **5,** 23–31.

Vernant, P., Nilfroushan, F., Hatzfeld, D., Abbassi, M., Vigney, C., Masson, F., Nankali, H. & Martinod, J., 2004. Contemporary Crustal Deformation and Plate Kinematics in Middle East constrained by GPS Measurements in Iran and North Oman, *Geophys. J. Int.,* **157,** 381–398.

Waldhauser, F. & Ellsworth, W.L., 2000. A double difference earthquake location algorithm: method and application to the northern Hayward fault, California, *Bull. seism. Soc. Am.,* **90,** 1353–1368.

Walker, R. & Jackson, J., 2002. Offset and evolution of the Gowk fault, S.E. Iran: a major intra-continental strike slip system., *J. Structural Geology,* **24,** 1677–1698.

Wang, R., Xia, Y., Grosser, H., Wetzel, H.U., Kaufmann, H. & Zschau, J., 2004. The 2003 Bam (SE Iran) earthquake: precise source parameters from satellite radar interferometry, *Geophys. J. Int.,* doi:101111/j.1365–246X.2004.02476.x

Wells, D.L. & Coppersmith, K.J., 1994. New Empirical Relationships among Magnitude, Rupture Lenth, Rupture Width, Rupture Area, and Surface Displacement, *Bull. seism. Soc. Am.,* **84,** 974–1002.

APPENDIX

Fig. A1 shows the lower hemisphere of the focal mechanisms.

Downloaded from https://academic.oup.com/gji/article/163/1/90/739453 by guest on 19 February 2021

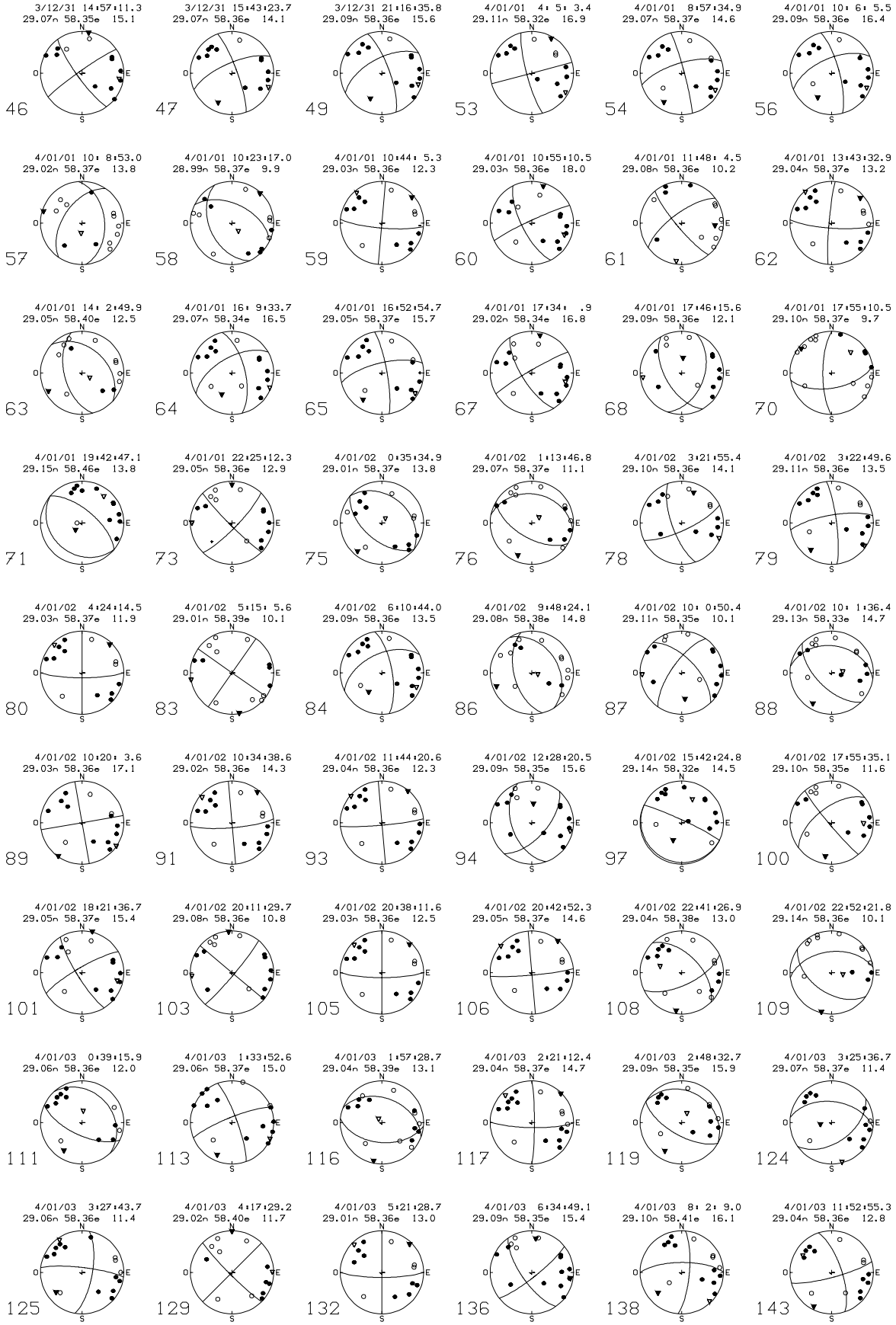

Figure A1. Lower hemisphere of the focal mechanisms. Solid- and open circles are reliable compressional and dilatational first motions, + and − are uncertain or weak. Solid triangles are *P*-axis and open triangles are *T*-axis.

Downloaded from https://academic.oup.com/gji/article/163/1/90/739453 by guest on 19 February 2021

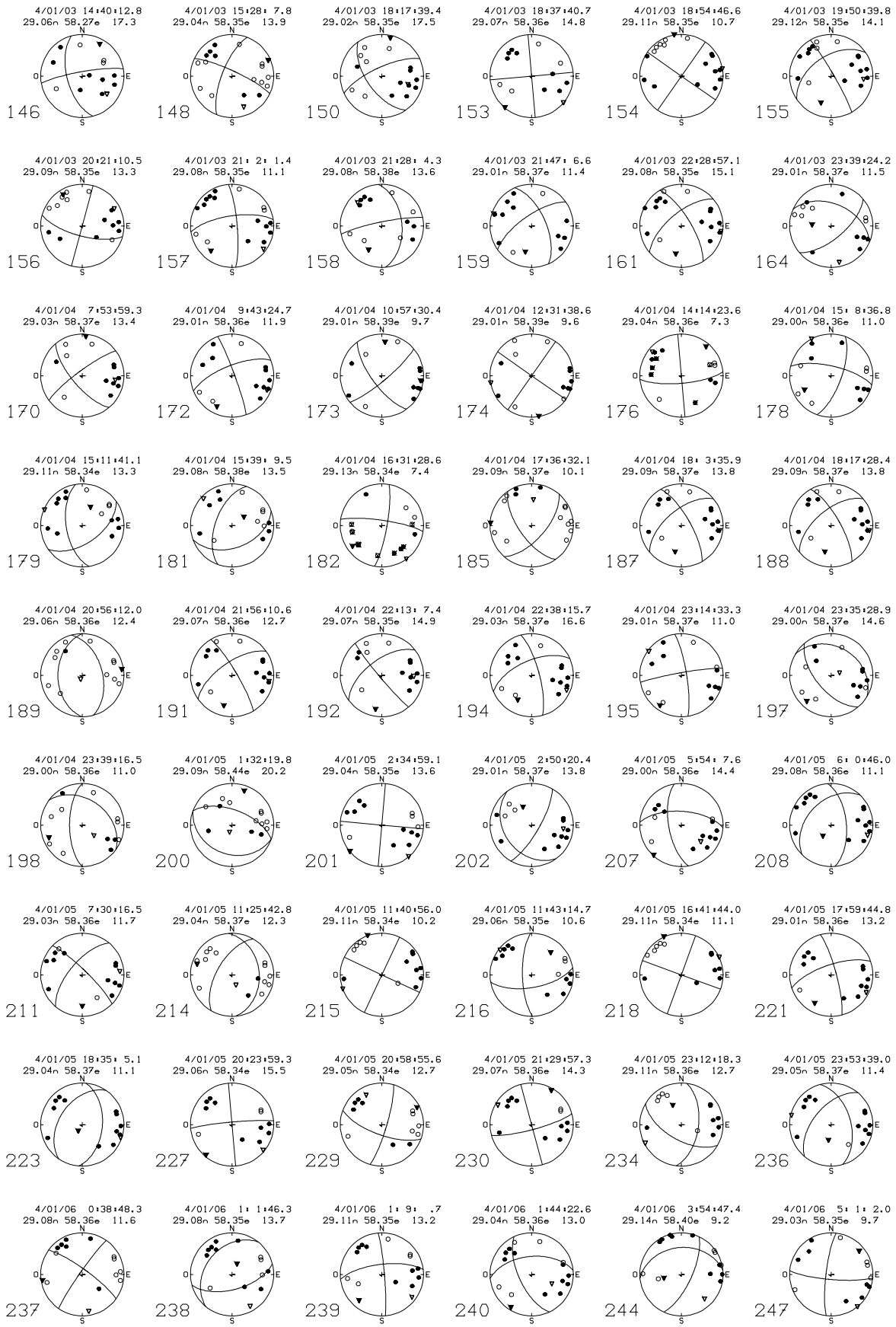

Figure A1 (*Continued.*)

Downloaded from https://academic.oup.com/gji/article/163/1/90/739453 by guest on 19 February 2021

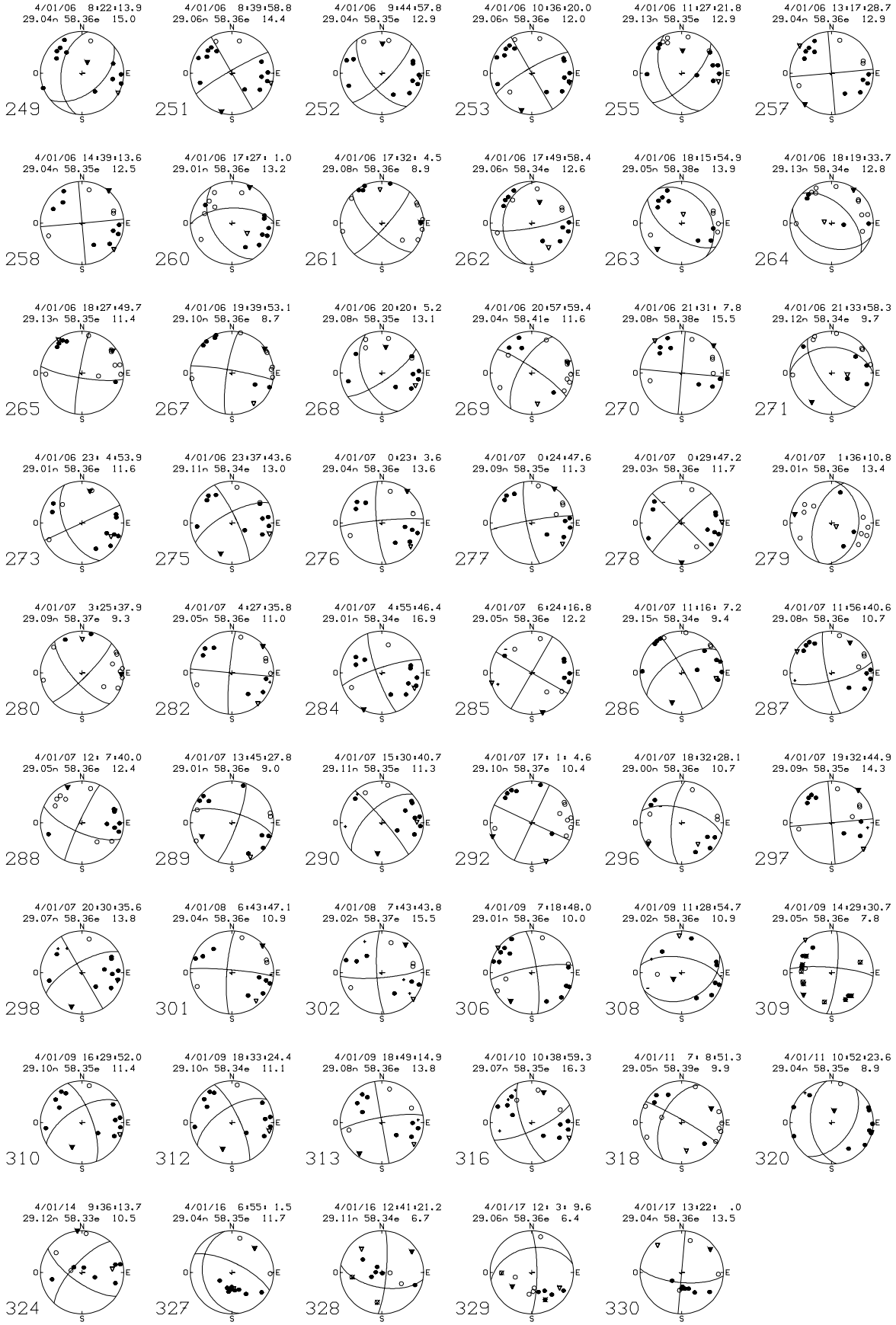

Figure A1. (*Continued.*)

Downloaded from https://academic.oup.com/gji/article/163/1/90/739453 by guest on 19 February 2021